ASSESSING THE IMPACT OF MOLTEN HALIDE SALTS ON CREEP OF STRUCTURAL ALLOYS AT 650°-750°C

Rishi Pillai and Bruce A. Pint
Materials Science and Technology Division, Oak Ridge National Laboratory, Oak Ridge, TN 37831-6156, USA

ABSTRACT

There is a critical lack of data on the mechanical behavior of candidate structural materials for advanced nuclear reactors under molten halide salt environments. Limited legacy data from the molten salt reactor experiment (MSRE) program showed a significant reduction in creep rupture strength of a Ni-base alloy in molten fluoride salt. With ongoing efforts to commercialize different molten salt reactor concepts, the industry can considerably benefit from quantitative information on the impact of molten halide salts on the engineering properties such as creep and fatigue strength of materials of interest. The present work aims to assess the role of molten salt corrosion on the creep behavior of three alloys 316H, 617 and 282 at 650-816 °C. Creep tests were conducted in fluoride (FLiNaK) and chloride (NaCl-$MgCl_2$) salts. Initial results from the ongoing testing will be presented which suggest that the molten salt environment caused a 25-50% reduction in creep rupture lifetime compared to air exposures. Physics-based corrosion and creep models were employed to gain some insights into the potential degradation mechanisms.

INTRODUCTION

Since the recent resurgence in the research and commercial interests in molten salt reactors (MSRs) as a viable advanced reactor concept to achieve the short- and long-term climate goals [1, 2], efforts to demonstrate their commercial potential are underway [3, 4]. These are relying on a combination of the extensive legacy knowledge from the molten salt reactor experiment (MSRE) [5] and relatively recent data on materials compatibility of structural materials of interest such as 316H in molten salts environments [6]**.** However, there are no long-term data equivalent to expected reactor operating durations (40 years) on the corrosion behavior of alloys of interest such as 316H, 617 and 709 in molten fluoride (FLiNaK or FLiBe) or chloride (NaCl-$MgCl_2$) salts. Furthermore, there are no experimental data on the short- or long-term impact of coupled extremes such as corrosion, stress and irradiation on the material degradation of these alloys. The 1958 report by Manly [7] had reported a significant influence of the molten fluoride salt NaF-ZrF_4-UF_4 (50-46-4 mol.%) environment on the creep behavior of a Ni-base alloy (Ni-15Cr-7Fe wt.%). The ongoing MSR commercialization efforts can benefit from relevant data on the engineering properties (e.g., creep and fatigue strength) of structural materials in molten salt environments.

The present work includes initial results on creep tests conducted for 316H in molten FLiNaK and NaCl-$MgCl_2$ salts and 617 in molten FLiNaK using hollow creep specimens. Baseline tests were conducted in air to assess the impact of the molten salts on the creep behavior Additionally, some data on the creep behavior of the γ′-strengthened Ni-base alloy 282 in molten chloride salts will also be included to provide some additional insights into the potential degradation mechanisms of creep-corrosion interactions. Preliminary microstructural characterization was conducted on the 316H and 282 specimens to derive correlations to the observed creep behavior. Coupled thermodynamic-kinetic modeling was employed to predict the salt corrosion induced compositional changes and phase transformations. A few preliminary calculations were performed with a previously developed physics-based continuum damage creep model to elucidate potential interactions between creep and corrosion degradation mechanisms.

EXPERIMENTAL PROCEDURE

The cylindrical hollow creep specimens had a 57.2 mm gage length, 12.7 mm outer and 11.2 mm inner diameter (ID). A stainless-steel cup made of type 316L stainless steel was attached to the bottom of the creep specimen to capture the molten salt after rupture. This specimen design was derived from a patent application [8]. All specimens were subjected to rigorous geometry checks in order to verify dimensions and surface finish. Particularly, the inner surface was electrical discharge machined (EDM) and polished to an R_a of 0.4 μm measured using a profilometer. Specimens of 316H were machined from a 2.54 cm thick 316H plate provided in a solution annealed state while specimens of 282 were machined from a 2.54 cm diameter rod subjected to the standard 2-step heat treatment of 282 (2h at 1010 °C → air cooled → 4h at 788 °C → air cooled). Alloy 617 specimens were machined from a 3.7 cm thick solution annealed plate provided by Thyssen Krupp VDM with an average grain size of 150 μm. The measured composition of the three alloys is given in Table 1.

Table 1: Compositions of the studied alloys in wt.% determined by plasma/combustion analyses

Alloy	Fe	Cr	Ni	Mn	Si	Mo	C	Co	Al	Ti	Other
316H	Bal.	16.6	10.3	1.6	0.3	2.0	0.04	0.2	-	-	Cu 0.4 N 0.03
617	1.6	22.2	Bal.	0.1	0.1	8.6	0.05	11.6	1.1	0.4	Cu 0.04
282	0.8	19.4	Bal.	-	-	8.5	0.06	10.2	1.5	2.2	Zr 0.01

The FLiNaK salt used for this work was prepared by a now defunct company Electrochemical Systems. The composition of the as-received salt was previously reported [6] . The NaCl–$MgCl_2$ eutectic salt used in this study was prepared with 58.5 mol% anhydrous NaCl salt and 41.5 mol% anhydrous $MgCl_2$ salt. The salt was homogenously mixed and purified following an established purification procedure for chloride salts [9]. The trace impurities of the NaCl–$MgCl_2$ eutectic salt mixture were identified by inductively coupled plasma mass spectrometry (ICP-MS) analysis [10] in which the most prominent impurity elements and the corresponding concentrations were 0.79 ppm Li, 5.44 ppm S, 15.7 ppm K, 6.99 ppm Ca, 0.03 ppm Cr, 0.01 ppm Mn, 0.13 ppm Fe, 0.23 ppm Ni (weight). The oxygen level in the salt was ~300-400 wppm.

The hollow creep specimens were filled in an Ar-filled glovebox (O_2 and H_2O < 0.1 ppm) with ~15 g of the salt and sealed by welding the cap (same material as the specimen) on the top in the glovebox. Before beginning the creep test, thermocouples were fixed at about 1/3 of the gauge length before threading on the catch cup. The completed load train (including the pull rods and specimen) was loaded into the furnace and threaded into the turn buckle before additional insulation was applied. The heating was 1 h to temperature followed by a 0.5 h hold to reach a steady state.

The system was operated within a 3 °C variance between the thermocouple on the specimen and the control thermocouple of the furnace. The linear variable displacement transducer (LVDT) used to measure displacement and derive creep strains was zeroed at this point and the specimen was loaded. The furnace was programmed to be switched off immediately upon specimen rupture to minimize corrosion damage to the specimen due to the leaking molten salt.

Post-exposure, specimens were cross-sectioned for metallographic analyses. The mounted samples were ground to 1200 grit with SiC grinding papers and subsequently polished with diamond pastes to 1 μm surface finish. Microstructural characterization to measure compositional changes and identify phase transformations was performed using scanning electron (SE), back-scattered electron (BSE) microscopy (TESCAN MIRA3 SEM) and energy dispersive x-ray spectroscopy (EDS:EDAX Octane Elect Super Silicon Drift Detector).

MODELING PROCEDURE

Corrosion modeling

A previously developed coupled thermodynamic-kinetic approach [11] was employed to model the simultaneously occurring corrosion, diffusion and dissolution processes in the alloy. The modified form of the modeling procedure to allow calculations to be run on parallel computing cores and thereby accelerate the simulations was utilized in the present work [12]. A detailed description of the modeling approach can be found in [11] but will be briefly described here for clarity.

The modeling approach is based on a 1D-finite volume discretization. The simulation begins by assigning each volume element in the computational domain with the corresponding local chemical composition. A geometric mesh was generated with a finer mesh at the alloy surface (left boundary) and gradually increasing cell size towards the specimen center (right boundary). The mesh was adapted at each time step since the domain would shrink due to corrosion induced loss of Cr from the base alloy. Thermodynamic and kinetic data were taken from the databases TCNi11 [13] and MobNi5 [14] respectively to calculate the chemical potentials and element mobilities that are used to calculate the flux of alloy constituents across the domain driven by chemical potential gradients. Diffusion was considered to occur only in the γ (disordered FCC) and γ′ (ordered FCC) phases. Overall, the phases γ-FCC, γ′- FCC, and carbides ($M_{23}C_6$, M_6C) were considered for the calculations. Wherever deemed essential (e.g., cold-worked surfaces, finer grain sizes < 100 μm), the alloy constituent mobilities M_c extracted from the mobility database (MOBNI5) were modified to M_c^{mod} in order to account for the grain-boundary assisted diffusion in the following manner:

$$M_c^{mod} = \frac{\delta}{d} M_c^{GB} + \left(1 - \frac{\delta}{d}\right) M_c \qquad \text{Eq. 1}$$

where M_c^{GB} is the mobility of constituent c in grain boundaries, δ is the grain boundary width, and d is the grain size.

The salt corrosion induced Cr and Fe loss was employed as a boundary condition on the alloy surface. The Cr loss kinetics for the investigated alloys were derived from previously measured dissolution rates of pure Cr in the KCl-$MgCl_2$ eutectic (68:32 mol.%) salt mixture [27] and recently measured values for Cr and Fe in FLiNaK [15] and in the binary NaCl-$MgCl_2$ eutectic salt mixture (will not be shown here for brevity). These loss kinetics are then scaled based on the chemical activity of Cr/Fe in the investigated alloys according to the previously described method [16].

Creep modeling

To predict the lifetime based on accumulated creep strains, a microstructure-based state-variable (or damage-mechanics) approach for improved design, based on a previously proposed procedure by Dyson and Mclean [17-19], was adopted to describe the creep behavior of the three alloys. The

method integrates contributions to creep damage by relevant degradation mechanisms (e.g., cavitation/cracking, particle coarsening, phase changes, dislocation accumulation)) allowing a material-specific evaluation of creep behavior). This is an advantage to empirical representations of creep behavior since an effective extrapolation to longer lives and more complex loading conditions requires that the differing mechanisms be integrated in the creep equations. Furthermore, this allows integration of corrosion-induced damage, e.g., depletion of the strengthening phase which can be critical for thin components and is relevant to the current work. A general description of the generic set of creep equations considering the relevant damage mechanism is given in Table 2. The overall creep strain rate $\dot{\boldsymbol{\varepsilon}}$ at a given stress σ is given by,

$$\dot{\varepsilon} = \frac{\dot{\varepsilon_0}}{1 - D_{\mathrm{d}}} sinh\left[\frac{\sigma(1-H)}{\sigma_0(1-D_{\mathrm{p}})(1-D_{\mathrm{sp}})}\right] \qquad \text{Eq. 2}$$

Table 2: Different damage mechanisms and corresponding rate equations

Equation	**Damage mechanism**
$\dot{H} = \frac{h'}{\sigma}\left(1 - \frac{H}{H^*}\right)\dot{\varepsilon}$	Strain hardening and recovery
$\dot{D_{\mathrm{d}}} = C_4(1 - D_{\mathrm{d}}^2)\dot{\varepsilon}$	Dislocation multiplication
$\dot{D_{\mathrm{p}}} = \frac{K_p}{3}(1 - D_{\mathrm{p}})^4$	Particle coarsening
$\dot{D_{\mathrm{sp}}} = \frac{K_{\mathrm{sp}}}{d^2 D_{\mathrm{sp}}}$	Corrosion induced loss in alloy strength (e.g., depletion of strengthening phases)
$\dot{\sigma} = \sigma\dot{\varepsilon}$	Stress change during constant load test; necking

A detailed description of the creep modeling approach, the symbols in Eq. 2 and the involved parameters such as strain hardening/recovery H, the intrinsic strain rate $\dot{\varepsilon_0}$ and the microstructural parameter σ_0 is given in [20]. In addition to the typically included damage mechanisms (e.g., dislocation multiplication and particle coarsening), dissolution of the strengthening phase has also been included here to account for the corrosion-induced dissolution of strengthening precipitate phases in the alloys chosen here. This might be a critical damage mechanism and be life-limiting for thin components (< 1.0 mm), with the depth of precipitate-denuded zones reaching up to 50% of the component thickness resulting in significant reduction in creep strength, especially in a molten salt environment. The system of differential equations given by the rate equations in Table 2 was solved and the solution was fitted to a subset of the measured creep data for 282 [21] using the global minimization genetic algorithm procedure in MATLAB.

RESULTS

Figure 1 shows the measured creep strains of 316H in air, FLiNaK and NaCl-$MgCl_2$ (Figure 1a) at 650 °C/160 MPa and 617 in air and FLiNaK at 750 °C/146 MPa (Figure 1b). The molten salt environ-

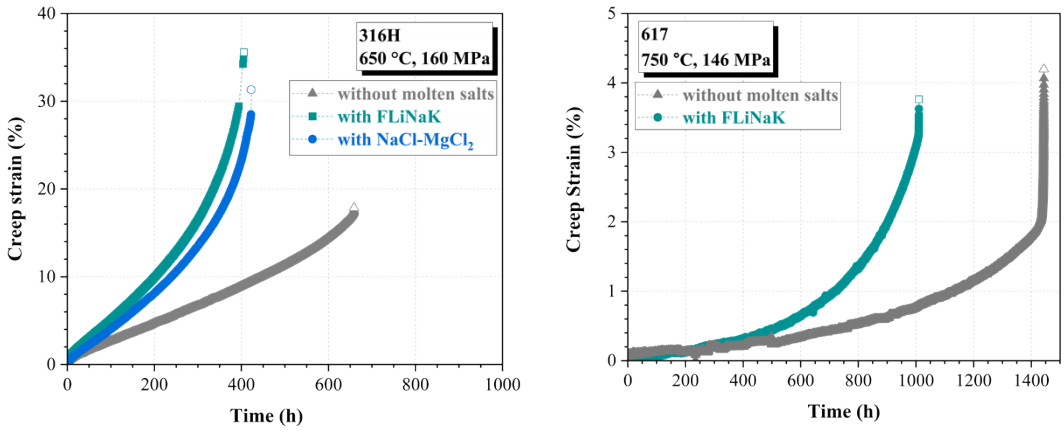

(a) (b)

Figure 1: Measured creep strains of (a) 316H in air, FLiNaK, NaCl-$MgCl_2$ and (b) 617 in air and FLiNaK. Open symbols indicate failure time.

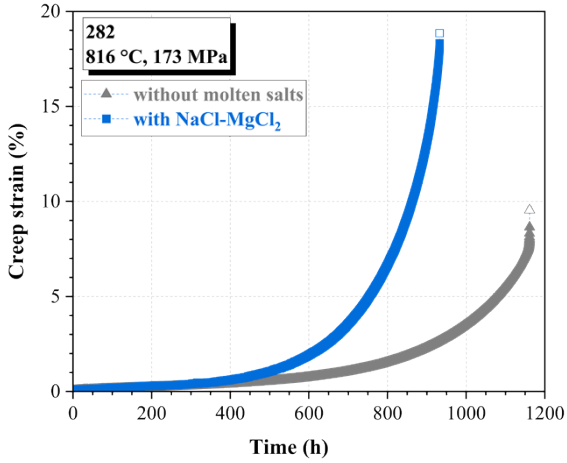

Figure 2: Measured creep strains of 282 in air and NaCl-$MgCl_2$. Open symbols indicate failure time.

ment has evidently reduced the creep rupture life of both the alloys compared to the baseline creep rupture lifetime in air. There does not seem to be a reduction in creep ductility due to the molten salt environment to suggest a brittle creep rupture. In fact, for 316H, the creep rupture strains in molten salts were higher than the corresponding tests in air. The creep strains were relatively low for both 617 specimens tested in air and FLiNaK compared to the data for 617 in the literature [22]. This might be due to the lower number of grains expected across the wall thickness of the current specimen geometry (0.76 mm) which is below the recommended wall thickness of 3.175 mm [22]. Figure 2 shows the measured creep strains of 282 in air and NaCl-$MgCl_2$ at 816 °C and 173 MPa. The specimen tested in FLiNaK showed a 25% reduction in creep rupture time but a higher creep rupture strain.

A closer look at the cross-sections of the area close to the corresponding fracture surfaces for the 316H specimens (Figure 3) shows that the exposure in NaCl-$MgCl_2$ resulted in the most severe attack with a significant reduction in the specimen thickness. A similar observation can be made for the 282 specimens with the creep specimen tested in the chloride salt showing a significantly higher metal loss than the specimen tested in air (Fig. 4).

The remaining metal thicknesses for all the specimens were measured and the results are summarized in Figure 5. The specimens tested in air showed a 15% reduction in wall thickness compared to the original wall thickness (760 μm) while the fluoride salt environment resulted in

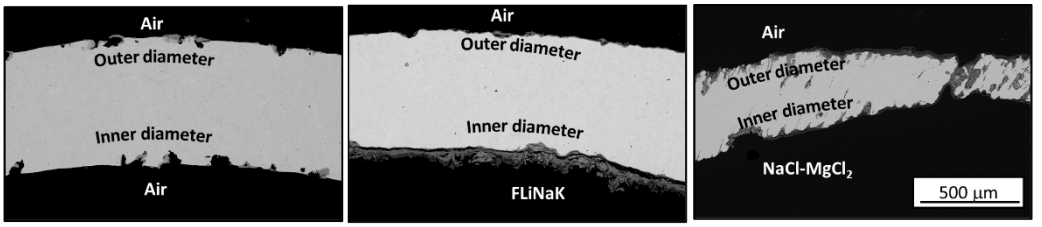

(a) (b) (c)

Figure 3: Backscattered secondary electron images of the cross-section of the fracture surfaces of 316H creep specimens tested (a) in air, (b) FLiNaK, and (c) NaCl-$MgCl_2$ at 650 °C and 160 MPa.

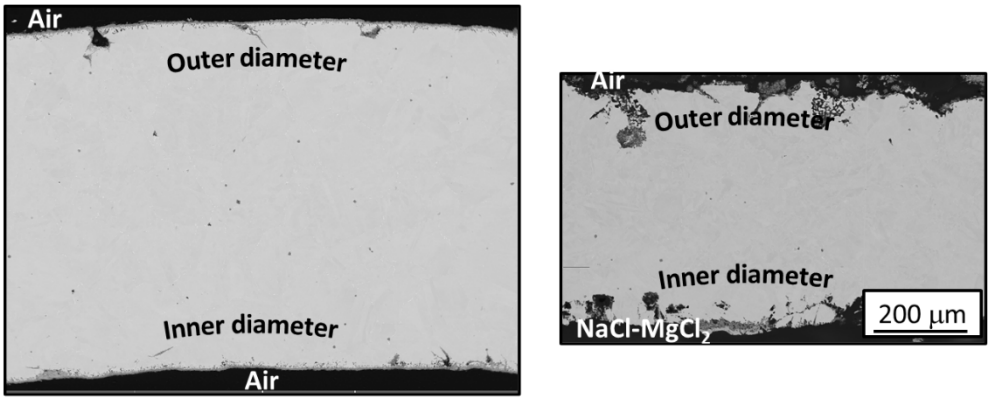

(a) (b)

Figure 4: Backscattered secondary electron images of the cross-section of the fracture surfaces of 282 creep specimens tested (a) in air and (b) NaCl-$MgCl_2$ at 816 °C and 173 MPa.

about a 30% reduction in wall thickness. In agreement with the images shown in Figure 3**Error! Reference source not found.**, the chloride salt showed a 60% loss in wall thickness. For 282, the creep specimen tested in NaCl-$MgCl_2$ showed a 40% metal loss. The measured concentration profiles for the alloying constituents near the fracture surface did not show the typically observed depletion profiles after exposure of these alloys to molten salts. This is most likely due to the rapid corrosion that occurs in the corrosion-affected zone once the specimen ruptures and the leaked salt comes in contact with the air. Furthermore, the strong corrosion attack observed for the NaCl-$MgCl_2$ mixture might have resulted in considerable metal loss that would have suppressed any noticeable elemental depletion, as was

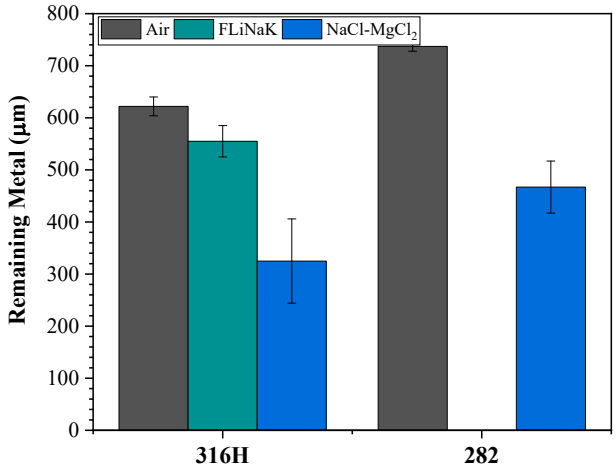

Figure 5: Measured thickness of the remaining metal of 316H creep specimens tested in air, FLiNaK and NaCl-$MgCl_2$ at 650 °C and 160 MPa.and 282 creep specimens tested in air and NaCl-$MgCl_2$ at 816 °C and 173 MPa. The values are an average of 20 measurements and the error bars represent one standard deviation.

observed by Wang et al. [10] for the case of 316H exposed in the same chloride salt. Consequently, no quantitative information about the corrosion-induced compositional changes in the alloys during the creep tests could be acquired. However, in one case the difference between air and molten salt exposures on the Cr depletion could be observed. Figure 6a compares the Cr concentration profile in 316H from the inner diameter (x=0) to the outer diameter after creep testing at 650 °C and 160 MPa in air and FLiNaK. The specimen exposed in air showed typical oxidation induced depletion profiles both at the inner and outer diameter. Although the outer diameter of the salt-filled specimen was exposed to air, the Cr concentration profile is relatively flat suggesting complete metal loss due to the leaked salt. A closer look near the inner diameter of the fluoride salt-filled specimen in Figure 6b shows remnants of a depletion profile.

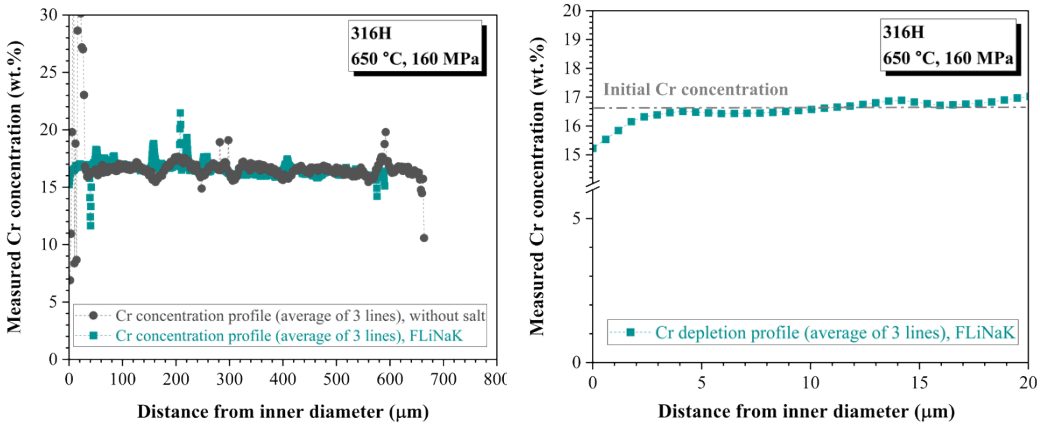

Figure 6: (a) Comparison of the measured Cr concentration profiles in 316H creep specimens tested in air and FLiNaK at 650 °C and 160 MPa, (b) a re-scaled Cr profile for the 316H creep specimen tested in FLiNaK.

DISCUSSION

The molten salt environment reduced the creep rupture life of all tested alloys. A comparison of the measured creep curves in air and molten salt shows that the molten salt environment is predominantly accelerating the transition to the tertiary creep regime. The primary and secondary creep regimes do not seem to be significantly affected. This suggests that the time dependence of the corrosion processes might be the most likely degradation mechanism accelerating creep. The creep tests conducted here are relatively short-term compared to the expected reactor operating lifetimes. If corrosion is accelerating the transition to the tertiary creep regimes, the impact of molten salts on creep rupture life may be considerably higher at lower stresses (longer creep lifetime) than observed here. Detailed microstructural characterization efforts are ongoing to provide some insights into the underlying mechanisms driving the accelerated degradation. However, the corrosion and creep models can aid in identifying potential causes.

Figure 7a shows the calculated Cr depletion profiles for the 316H creep specimen tested in FLiNaK under the assumption that stress does not accelerate corrosion in the molten salt. The calculated depth of corrosion is about 30 µm after 400 h (close to the creep rupture time of the specimen, Figure 1a). The temporal evolution of the Cr and Fe loss from the specimen is given in Figure 7b. The saturation limits for Cr and Fe were calculated from the amount of salt in the creep specimen and the dissolution contents measured for pure Cr and Fe in the chemically identical FLiNaK respectively. For a test duration of 400 h, the Cr and Fe dissolution from 316H at 650 °C are far from their respective saturation limits suggesting that corrosion was expected to continue throughout the duration of the test.
In contrast, the calculated depth of corrosion for 316H in NaCl-$MgCl_2$ was about 50 µm after 400h accompanied by a metal loss of about 20 µm (Figure 8a). This is expected given the much higher dissolution rates measured for pure Cr and Fe in the chloride salt. Consequently, the calculated elemental loss rates and amounts of Cr and Fe from 316H shown in Figure 8b are significantly higher than in the FLiNaK case. Fe dissolution is expected to be saturated after 500h and very close to its saturation limit after 400h while Cr will most likely continue to be depleted from the alloy even after 1000h. The high Fe loss from 316H can be expected to result in significant metal loss compared to FLiNaK and the micrographs and corresponding metal loss measurements shown in Figure 3 and Figure 5 respectively provide partial evidence for this prediction. The operation of a 316H microloop in NaCl-$MgCl_2$ (chemically similar salt provided by ORNL) resulted in clogging of the loop only after 260h due to the redeposition of the elements depleted from the hot leg section in the cold leg [10]. The measured depth of corrosion attack in that case was 10-20 µm after 260 h in the hot leg (620 °C) and the calculated corrosion depth after 200 h at 650°C in the present work is 25 µm suggesting that the model predictions in the present work are plausible.

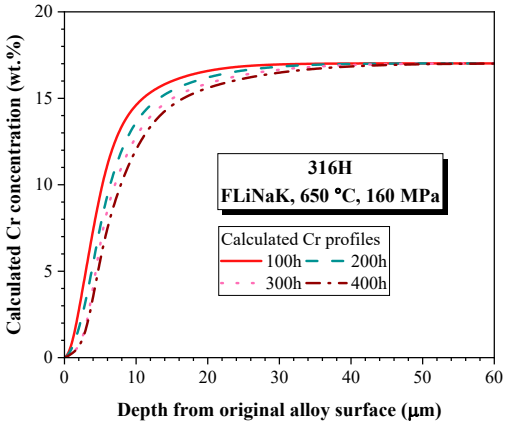

(a)

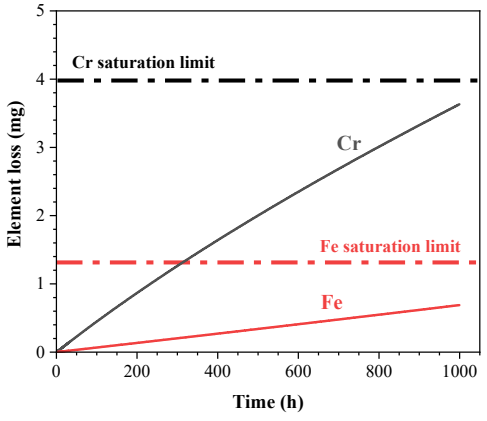

(b)

Figure 7: (a) Calculated Cr depletion profiles for 316H creep specimens tested in FLiNaK, and at 650 °C and 160 MPa, (b) corresponding calculated time evolution of Cr and Fe depletion from the alloy.

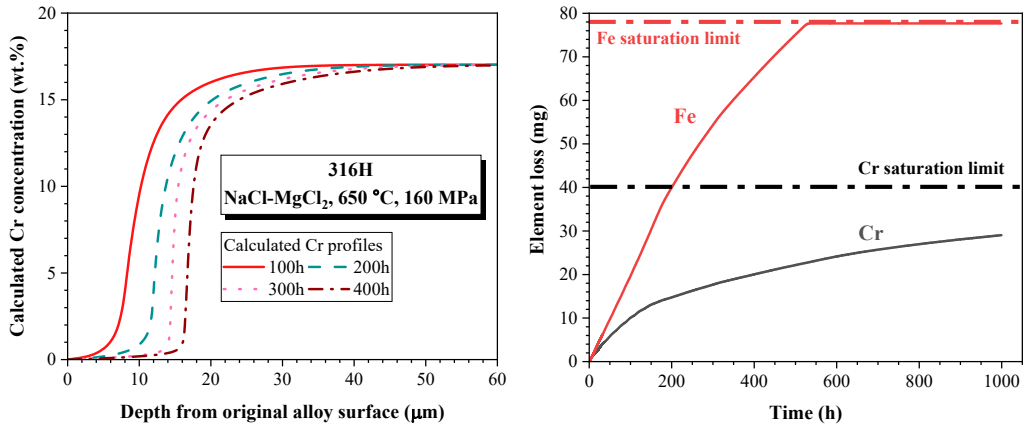

(a) (b)

Figure 8: (a) Calculated Cr depletion profiles for 316H creep specimens tested in $NaCl\text{-}MgCl_2$, at 650 °C and 160 MPa, (b) corresponding calculated time evolution of Cr and Fe depletion from the alloy.

Although the depth of corrosion attack was predicted to be higher in the chloride than the fluoride salt, the creep rupture times of 316H were similar for both. This result might be hinting toward one or more critical corrosion-induced microstructural changes. In these early stages of investigation in the present study, no guidance can be derived from the very limited studies on the impact of stress-corrosion interactions in molten salts. Gu et al. [23] studied the stress-assisted corrosion behaviour of Hastelloy N in FLiNaK salt under 4-point bending. The authors concluded that selective diffusion of Cr at the grain boundaries (GBs) of the Ni-base alloy Hastelloy N made these sites susceptible to further corrosion crack. Stress further promoted Cr diffusion and accelerated GB carbide precipitation, thereby forming a corrosion couple between the carbide and matrix that facilitated the expansion of intergranular corrosion cracks into the grains. However, the experimental evidence provided by the authors was not conclusive. Furthermore, the test crucible containing the salt was made of graphite which can react with the test specimen and fixtures (made out of 316 SS) and result in non-negligible effects and incorrect conclusions. Manly et al. [7] had suggested the dissolution of carbides driven by the corrosion-induced Cr depletion, along with the subsurface void formation, as reasons for the deterioration in creep strength of the Ni-base alloy (Ni-15Cr-7Fe wt.%) creep tested in $NaF\text{-}ZrF_4\text{-}UF_4$ (50-46-4 mol.%) salt. The mechanism of carbide dissolution and back-diffusion toward the specimen core due to Cr depletion has been experimentally [24] and computationally [25] demonstrated previously and is expected to occur in all three tested alloys. The correlation between this phenomenon and the observed creep behavior of 316H and 617 in the present study remains to be elucidated.

For the case of 282, the measured metal loss of about 10 μm (Figure 5) for creep specimen tested in air after ~1200 h agreed well with the expected metal loss due to oxidation. Based on the experimentally known temperature dependence of parabolic oxidation rates of 282 [26], the oxidation-induced metal loss was calculated to be 9 μm at 816 °C after 1200 h. The exposure in $NaCl\text{-}MgCl_2$ was predicted to result in a corrosion depth of about 50 μm after 1000 h with a maximum loss in sound metal of 5 μm as shown in Figure 9a with the help of Cr depletion profiles. The time evolution of the Cr loss from 282 plotted in Figure 9b shows that the amount of Cr calculated to deplete from the creep specimen is far from its saturation limit in the salt after 1000 h at 816 °C suggesting continued corrosion throughout the duration of the creep test. The negligible

amount of Fe (0.3 wt.%) in 282 meant that the alloy was resistant to considerable metal loss compared to 316H despite the higher test temperature.

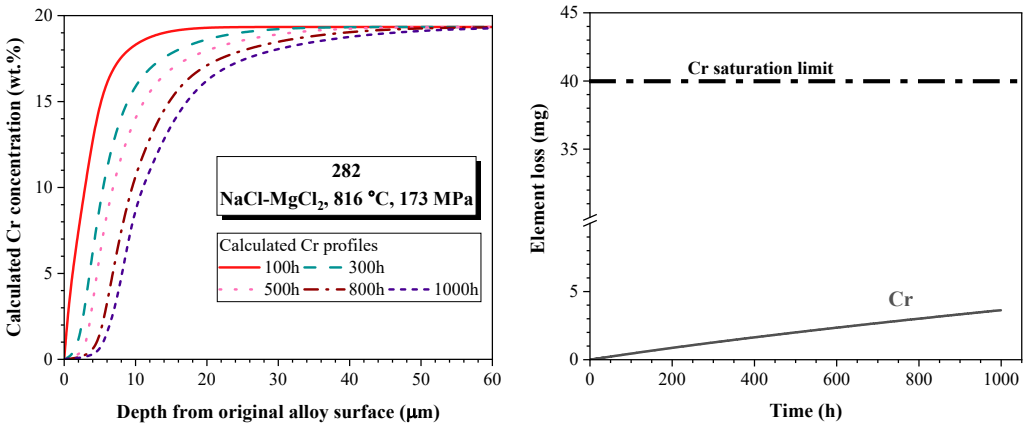

(a) (b)

Figure 9: (a) Calculated Cr depletion profiles for 282 creep specimens tested in NaCl-$MgCl_2$, at 816 °C and 173 MPa, (b) corresponding calculated time evolution of Cr and Fe depletion from the alloy.

It is worth mentioning here that the model assumes exclusive depletion of Cr from 282 but other elements such as Al, Ti and Co have been observed to be depleted from the γ′-strengthened Ni-base alloy 740H after exposures in chloride salts [16, 27]. Al and Ti are γ′-stabilizing elements and their limited depletion from the alloy (as little as 0.1 wt..%) combined with the significant Cr depletion (Figure 9) can dissolve γ′ (based on previous work [28] and thermodynamic calculations performed in the present study) and weaken the corrosion affected alloy subsurface accelerating creep strain rates. If these increased creep strains further drive transport of these elements from the alloy beyond the corrosion affected zone through stress-induced vacancy migration, the cycle of stress-corrosion interactions can repeat until failure. The depth of the oxidation-induced γ′ dissolution in 282 for an air exposure is expected to be about 20 µm after 1000h at 816 °C based on the temperature dependence of the γ′-dissolution rates derived in [20], which in this case also corresponds to the parameter K_{sp} in
Table 2. Based on the results in Figure 9, the exposure in the chloride salt will potentially double the depth of the γ′-denuded zone and thereby accelerating creep failure. The simultaneous loss of Al and Ti from 282 is not considered in the model due to the lack of data on the dissolution of these elements in the salts of interest. In the present calculations, the Cr depletion drives enrichment of Al and Ti in the alloy subsurface which would increase the γ′ phase fraction and retard Cr transport due to its slower diffusion in γ′. With this fact in mind, it can be concluded that the model is most likely underestimating the Cr loss from the alloy.

The creep model described earlier can be employed to evaluate the impact of corrosion on creep. The model was previously developed to describe creep behavior of alloys 740H and 282 considering the simultaneous impact of air oxidation [20]. The creep data used to estimate key model parameters was extracted from respective code cases of the alloys [21, 29]. The same model was used here to predict the creep behavior of the hollow 282 creep specimen and the comparison between measured and calculated creep strains is given in Figure 10a. The good agreement even for a non-standard specimen geometry validates the applicability of the creep model in this case. Considering the impact of molten salt corrosion on the inner surface of the hollow specimen and assuming that the entire corrosion affected zone will degrade creep properties, e.g., through complete dissolution of γ′ in the alloy subsurface of 282, the creep curve for exposure in NaCl-

$MgCl_2$ was calculated and plotted along with the measured creep curve in Figure 10a. The model correctly predicted the decrease in creep rupture behavior both qualitatively and quantitatively. A closer look at the time evolution of the damage parameters between the air and chloride salt exposures (Figure 10b) shows that the damage parameter corresponding to the corrosion induced loss

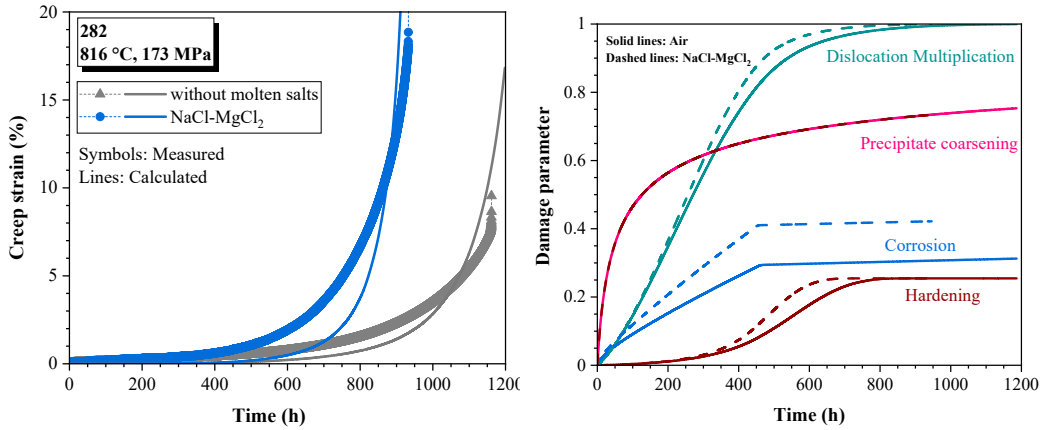

(a) (b)

Figure 10: (a) Comparison between measured and calculated creep strains of 282 in air and NaCl-$MgCl_2$ at 816 °C and 173 MPa, (b) corresponding comparison of the time evolution of the creep damage parameters in Eq. 2.

in creep strength $\boldsymbol{D}_{sp}$ is about 40% higher for chloride salts. The creep modeling results are encouraging and seem to suggest a plausible degradation mechanism. However, this needs to be experimentally verified through microstructural characterization.

CONCLUSIONS

Initial results on the creep behavior of the austenitic steel 316H, the solid solution-strengthened Ni-base alloy 617 and the precipitation strengthened Ni-base alloy 282 in molten fluoride (FLiNaK) and chloride (NaCl-$MgCl_2$) salts were presented and discussed. The molten salt environment resulted in a decrease in the creep rupture life of all alloys. The creep behavior of 316H at 650 °C and 160 MPa was similarly affected by fluoride and chloride salts with nearly identical times to failure. The exposure of 617 in the fluoride salt resulted in about a 30% reduction in creep rupture time while exposure in chloride salt resulted in a 25% reduction in creep rupture time for 282. With the help of a coupled thermodynamic-kinetic model, it could be shown that corrosion in the chloride salt is most detrimental and will most likely result in significantly higher metal losses for 316H, a result which was partially supported by experimental observations. The continuum damage creep model was able to show that molten salt corrosion can decrease the creep rupture life in the case of 282 under the assumption that the corrosion drives depletion of the strengthening γ′-phase.

ACKNOWLEDGMENTS

B. Johnston, J. Wade, A. Willoughby and K. Epps assisted with the experimental work at ORNL D. Newberry. T. Lowe and M. Romedenne are thanked for helping with metallography and microstructural characterization. S. Bell and R. Mackenzie are thanked for their valuable comments on the paper. This research was sponsored by the US Department of Energy Office of Nuclear Energy, Molten Salt Reactor Campaign, the Nuclear Energy Advanced Modeling and Simulation

program and the Laboratory Directed Research and Development Program of Oak Ridge National Laboratory, managed by UT-Battelle, LLC, for the U. S. Department of Energy.

REFERENCES

[1] Locatelli, G., Mancini, M., Todeschini, N., "Generation IV nuclear reactors: Current status and future prospects," *Energy Policy*, Vol. 61 (2013) pp. 1503-1520.
[2] Serp, J., et al. The molten salt reactor (MSR) in generation IV: Overview and perspectives, *Progress in Nuclear Energy*, Vol. 77 (2014) pp. 308–319.
[3] Zhao, H., L. Fick, A. Heald, Q. Zhou, S. Richesson, N. Sutton, B. Haugh, Development, Verification, and Validation of an Advanced Systems Code KP-SAM for Kairos Power Fluoride Salt–Cooled High-Temperature Reactor (KP-FHR), *Nuclear Science Engineering*, Vol. 197 (2023) pp. 813-839.
[4] Kelleher, B. C., Gagnon, S. F., Mitchell, I. G., Thermal gradient mass transport corrosion in NaCl-$MgCl_2$ and $MgCl_2$-NaCl-KCl molten salts, *Materials Today Communications*, 33 Vol. (2022) 104358.
[5] Macpherson, H. G., Development of Materials and Systems for Molten-Salt Reactor Concept, *React Technol*, Vol. 15 (1972) pp. 136-155.
[6] Raiman, S.S., et al., Corrosion of 316H stainless steel in flowing FLiNaK salt, *Journal of Nuclear Materials*, Vol. 561 (2022) 153551.
[7] Manly, W. D., et al., AIRCRAFT REACTOR EXPERIMENT--METALLURGICAL ASPECTS, ORNL report, ORNL-2349 Oak Ridge, TN 1958.
[8] Ren, W., Molten salt environment creep testing extensometry system, U.S. Patent Office application WO2018152104A1, 2018.
[9] Mayes, R. T., J.M. Kurley Iii, P.W. Halstenberg, A. McAlister, D. Sulejmanovic, S.S. Raiman, S. Dai, B.A. Pint, Purification of Chloride Salts for Concentrated Solar Applications, ORNL Report ORNL/LTR-2018/1052, Oak Ridge, TN, 2018.
[10] Wang, Y., A.P. Olson, C. Falconer, B. Kelleher, I. Mitchell, H. Zhang, K. Sridharan, J.W. Engle, A. Couet, Radionuclide tracing based in situ corrosion and mass transport monitoring of 316L stainless steel in a molten salt closed loop, *Nature Communication*, Vol. 15 (2024) p. 3106.
[11] Pillai, R., W.G. Sloof, A. Chyrkin, L. Singheiser, W.J. Quadakkers, A new computational approach for modelling the microstructural evolution and residual lifetime assessment of MCrAlY coatings, *Materials at High Temperature*, Vol. 32 (2015) pp. 57-67.
[12] Pillai, R., T. Galiullin, A. Chyrkin, W.J. Quadakkers, Methods to increase computational efficiency of CALPHAD-based thermodynamic and kinetic models employed in describing high temperature material degradation, *CALPHAD*, Vol. 53 (2016) pp. 62-71.
[13] Thermo-Calc, Thermo-Calc Software TCNi11/Ni-alloys database v.11.0, 2021.
[14] MobNi5, Thermo-Calc Software MobNi5/Ni-alloys mobility database v.5, Sweden, 2019.
[15] Pint, B. A., D. Sulejmanovic, R. Pillai, Measuring the Dissolution of Cr and Fe at 550°-750°C in FLiNaK and FLiBe, ORNL Report, ORNL/SPR-2023/3169, Oak Ridge, TN, 2023.
[16] Pillai, R., D. Sulejmanovic, T. Lowe, S. Raiman, B.A. Pint, Establishing a design strategy for corrosion resistant structural materials in molten salt technologies, *JOM*, Vol. 75 (2023) 994-1005.
[17] McLean, M., B.F. Dyson, Modeling the effects of damage and microstructural evolution on the creep behavior of engineering alloys, *J Eng Mater-T Asme*, Vol. 122 (2000) pp. 273-278.
[18] Dyson, B. F., Osgerby, S., Modeling Creep Corrosion Interactions in Nickel-Base Superalloys, *Material Science and Technolology*, Vol. 3 (1987) pp. 545-553.
[19] Dyson, B., Use of CDM in materials modeling and component creep life prediction, *J Press Vess-T Asme*, Vol. 122 (2000) pp. 281-296.
[20] Pillai, R., M. Romedenne, S. Lee, Development of an Open-source Alloy selection and Lifetime assessment tool for structural components in CSP, ORNL/TM-2021/2365, 2022.
[21] Pint, B. A., H. Wang, C.S. Hawkins, K.A. Unocic, Technical Qualification of New Materials for High Efficiency Coal-Fired Boilers and Other Advanced FE Concepts: Haynes® 282® ASME

Boiler and Pressure Vessel Code Case, Oak Ridge National Lab. (ORNL), Oak Ridge, TN (United States), 2020, pp. 31.
[22] Wright, R. N., Draft ASME Boiler and Pressure Vessel Code Cases and Technical Bases for Use of Alloy 617 for Constructions of Nuclear Component Under Section III, Division 5, 2021.
[23] Gu, Y., W. Zhang, Y. Xu, Y. Shi, K. Volodymyr, Stress-assisted corrosion behaviour of Hastelloy N in FLiNaK molten salt environment, *npj Materials Degradation*, Vol. 6 (2022) p. 90.
[24] Ennis, P. J., W.J. Quadakkers, H. Schuster, Effect of Selective Oxidation of Chromium on Creep Strength of Alloy-617, *Materials Science and Technology*, Vol. 8 (1992) pp. 78-82.
[25] Chyrkin, A., R. Pillai, H. Ackermann, H. Hattendorf, S. Richter, W. Nowak, D. Grüner, W.J. Quadakkers, Modeling carbide dissolution in alloy 602 CA during high temperature oxidation, *Corrosion Science*, Vol. 96 (2015) pp. 32–41.
[26] Romedenne, M., R. Pillai, S. Dryepondt, B. Pint, The Impact of Oxidation-Induced Degradation on Materials Used in H_2-Fired Microturbines, *J. Eng. Gas Turb Power*, Vol. 146 (2024).
[27] Pint, B. A., Y.F. Su, D. Sulejmanovic, R. Pillai, Characterization of Fe and Cr Dissolution and Reaction Product Formation in Molten Chloride Salts With and Without Impurities, *Mater. High Temp.*, Vol. 40 (2023) pp. 360-370.
[28] Romedenne, M., A. Haynes, R. Pillai, Cyclic oxidation behavior of selected commercial NiCr-alloys for engine exhaust valves in wet air environment between 800 and 950 °C, *Corrosion Sci*ence, Vol. 211 (2023) 110817.
[29] Render, R., M.L. Santella, X. Chen, P.F. Tortorelli, V. Cedro, Long-Term Creep-Rupture Behavior of Alloy Inconel 740/740H, *Metalurgical and Materials Trans A*, Vol. 52 (2021) p. 3669.